On subducting slab entrainment of buoyant asthenosphere

J. Phipps Morgan,[1] Jörg Hasenclever,[2,3] M. Hort,[3] L. Rüpke[2,4] and E. M. Parmentier[5]

[1]*Department of Earth and Atmospheric Sciences, Cornell University, Ithaca, NY, USA;* [2]*IfM-GEOMAR, Kiel University, Kiel, Germany;* [3]*Institute of Geophysics, Hamburg University, Hamburg, Germany;* [4]*Department of Physics, PGP, Oslo University, Oslo, Norway;* [5]*Department of Geological Sciences, Brown University, Providence, RI, USA*

ABSTRACT

Laboratory and numerical experiments and boundary layer analysis of the entrainment of buoyant asthenosphere by subducting oceanic lithosphere implies that slab entrainment is likely to be relatively inefficient at removing a buoyant and lower viscosity asthenosphere layer. Asthenosphere would instead be mostly removed by accretion into and eventual subduction of the overlying oceanic lithosphere. The lower (hot) side of a subducting slab entrains by the formation of a ~10–30 km-thick downdragged layer, whose thickness depends upon the subduction rate and the density contrast and viscosity of the asthenosphere, while the upper (cold) side of the slab may entrain as much by thermal 'freezing' onto the slab as by mechanical downdragging. This analysis also implies that proper treatment of slab entrainment in future numerical mantle flow experiments will require the resolution of ~10–30 km-thick entrainment boundary layers.

Terra Nova, 19, 167–173, 2007

Introduction

Typical cartoons of mantle convection show oceanic lithosphere moving in concert with the underlying mantle flow (Fig. 1a). If, however, the asthenosphere layer – presumed to underlie at least much of the oceanic lithosphere – is itself less dense and viscous than the underlying mantle, then the resulting asthenosphere circulation can be strongly altered in ways that may have significant geological consequences (Fig. 1b,c). Here, we study the question of how efficiently a subducting slab will entrain buoyant asthenosphere near a subduction zone, a question that leads to a better understanding of the behaviour of the asthenosphere–lithosphere system in mantle convection.

There exist several different views on what exactly is asthenosphere. Seismic observations of the radial Earth structure show a low-seismic-velocity (Dziewonski and Anderson, 1981) and high attenuation (Widmer *et al.*, 1991) layer between ~100 and 300 km depths. This layer with low seismic wavespeeds is now known to be well developed beneath the ~60–100 km-thick oceanic lithosphere (Gaherty *et al.*, 1999) and active young continental margins such as

Correspondence: J. Phipps Morgan, Department of Earth and Atmospheric Sciences, Cornell University, Ithaca, NY USA. Tel.: +1 607-821-1741; fax: +1 607-254-4780; e-mail: jp369@cornell.edu

the Basin and Range (Goes and van der Lee, 2002) in the western U.S. However, beneath stable continental regions such as the Archaean shields in W. Australia (Gaherty *et al.*, 1999) and N. America (Goes and van der Lee, 2002) seismic wavespeeds are significantly faster, implying the presence of much stronger (lithospheric) mantle between 60 and 250 km depths (see also Gung *et al.*, 2003). The LVZ is an observed fact. Most researchers believe the LVZ also corresponds to a lower viscosity region within Earth's mantle. Rock-mechanics arguments, for example, imply the existence of a low-viscosity zone at the shallowest hot mantle where competing temperature and pressure effects lead to a viscosity minimum (Weertman and Weertman, 1975; Buck and Parmentier, 1986; Karato and Wu, 1993). Studies of the distribution of stresses in the oceanic plates require a low viscosity asthenosphere of 10^{18}–10^{19} Pa-s underneath the ocean lithosphere (Richter and McKenzie, 1978; Wiens and Stein, 1985), consistent with the ~10^{18}–10^{19} Pa s viscosities inferred from post-glacial rebound at Iceland (Sigmundsson and Einarsson, 1992).

Several potential mechanisms have been suggested to cause the formation of a shallow asthenosphere layer with low wavespeeds, high attenuation and reduced viscosity. Silicate mantle close to its melting temperature will have slower wavespeeds, higher attenuation (Faul and Jackson, 2005), and lower viscosity (Weertman and Weertman,

1975; Karato and Wu, 1993) than it does as cooler temperatures. As the uppermost suboceanic mantle is closest to its solidus temperature, the asthenosphere could simply be a consequence of this effect, and the presence of any partial melt would enhance the reduction in viscosity (Hirth and Kohlstedt, 1995) and seismic wavespeeds (Hammond and Humphreys, 2000). A higher water content has also been suggested to be the origin for the LVZ (Karato and Jung, 1998), and to lead to a viscosity reduction in this region of the mantle (cf. Hirth and Kohlstedt, 1996).

We favour the hypothesis that Earth's asthenosphere forms as a simple consequence of mantle plume upwelling – as hot buoyant plume material naturally tends to rise, upwelling plumes bring hot buoyant material to the 'ceiling' of the convecting mantle that is formed by the base of the mechanical lithosphere (Phipps Morgan *et al.*, 1995a). In this case, asthenosphere material will actually be hotter than the underlying mantle (at least in terms of its potential temperature; e.g. temperature corrected for adiabatic effects). If the asthenosphere's average temperature is that of hot upwelling plumes, then an observation of the deflection of the 410- and 660-km discontinuities beneath Iceland suggests that it may be ~10–20% (i.e. ~150–300°C) warmer than the underlying ambient mantle (Shen *et al.*, 1996). This would result in a ~0.5–1% reduction in density of

....
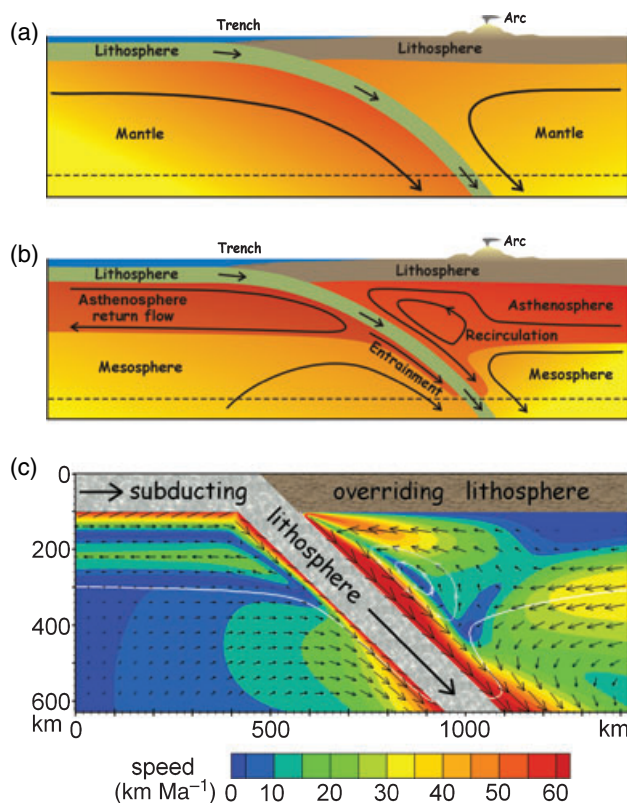
Fig. 1 (a) Cartoon illustrating the 'typical' connection of lithospheric plate motions with deeper mantle flow. (b) Cartoon illustrating the possible connection between plate motions and deeper flow when a buoyant low-viscosity asthenosphere decoupling zone is present. (c) A snapshot after 7 Ma from a numerical experiment discussed in the text that shows the behaviour illustrated in (b). Here the white line marks the boundary of asthenosphere material – a gradational asthenosphere–mesosphere transition (centred around 300 km depth) was made by having the asthensosphere–mesosphere interface conductively cool for 50 Ma in a static configuration before surface plate motions were 'turned on'. The oceanic lithosphere and slab are assumed to move at 63 km Ma^{-1}. White streamlines in the mantle wedge show the recirculation that develops in this region, colours show asthenosphere and mesosphere speeds, and arrows show instantaneous flow directions. (The experiments with a gradational asthenosphere–mantle interface evolve quite similarly to previous experiments in which this transition was assumed to be discontinuous, as seen by comparing the evolution of supplementary videos *oceanside.mpg* and *oceanside_sharp.mpg*.) The asthenosphere return flow beneath the base of the oceanic lithosphere is in good agreement with Schubert and Turcotte's (1972) simple boundary layer model, a boundary layer theory for the entrainment around the slab is discussed in Box 1.

the asthenosphere in comparison with the underlying cooler mantle ($\Delta\rho/\rho = \alpha\Delta T$, with $\alpha \sim 3.3 \times 10^{-5}$ °C^{-1}). Any partial melt extraction from upwelling plumes will actually increase the buoyancy of plume material while transforming some of the plume's thermal buoyancy into compositional depletion buoyancy. This happens because the increase in depletion buoyancy from melt-extraction in the garnet stability field (Boyd and McCallister, 1976; Oxburgh and Parmentier, 1977; Jordan, 1979) is roughly three times

larger than the decrease in thermal buoyancy due to cooling associated with the latent heat of partial melting (cf. Phipps Morgan *et al.*, 1995b). Depletion buoyancy would also arise from the preferential melting of denser and lower-solidus eclogite veins within an eclogite–peridotite 'marblecake' mantle.

If both hotter and shallower than the underlying mantle, the asthenosphere would also be much weaker. Karato and Wu's (1993) summary of the rheology of the uppermost mantle suggests that, for the most probable

viscous deformation mechanism in the uppermost mantle, dislocation creep of olivine at 1600 K, a 200 K increase in temperature leads to a > 100-fold viscosity reduction.

Numerical and laboratory experiments of asthenosphere slab-entrainment

We first discuss several numerical experiments that explore the entrainment surrounding a subducting slab. The key question we are interested in is how much asthenospheric material is downdragged by subducting slabs. Focusing on the effects of subduction processes, we also exclude mantle plumes as part of the numerical modelling domain. In order to highlight the implications of a hot and depleted, hence weak and buoyant asthenosphere layer we have simplified our setup for the numerical calculations in that phase transitions and melting processes are not considered. Instead, we begin with a preexisting 200 km-thick asthenosphere layer with a higher temperature and more depletion than the underlying mantle and ask how quickly it can be removed by plate subduction.

Consider the buoyant asthenosphere entrainment scenario sketched in Fig. 1(b) and Box 1. Intuition suggests a simple flow pattern may form, and this pattern is in fact seen in the numerical and laboratory experiments. The moving plate tends to drag shallower asthenosphere towards the subduction zone, which creates a relative pressure high that, in turn, locally tilts the asthenosphere base and drives deeper lateral asthenosphere flow away from the subduction zone as discussed in previous studies (Schubert and Turcotte, 1972; Phipps Morgan and Smith, 1992). In addition, the subducting slab tends to drag thin sheets of asthenosphere into the deeper mantle at its top and bottom boundaries (Fig. 1b,c). All of these effects are clearly visible in our numerical (Figure 1c) and laboratory (bottom-side only) experiments (Figure 3) as well as in the supplementary videos.

The numerical experiments were carried out in two dimensions with a code that uses a penalty finite-element formulation to determine viscous flow, a Smolarkiewicz-upwind-finite difference technique to solve for the thermal advection–diffusion problem, and
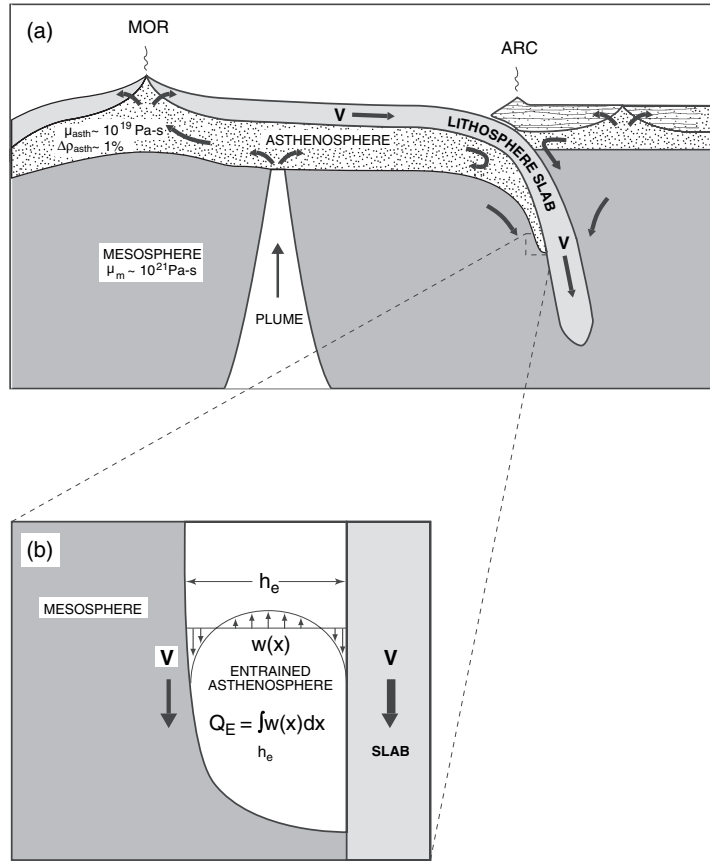
Box 1 (a) Cartoon of Earth's lithosphere, asthenosphere and mesosphere flow. To estimate the rate of asthenosphere entrainment by a subducting slab, we treat the entrainment process as the Poiseuille flow problem sketched in (b). The slab and adjacent mesosphere drag down a sheet of buoyant asthenosphere at a flux Vh, where V is the vertical speed of the downgoing slab and h is the thickness of the entrained asthenosphere sheet. Within the sheet itself, local buoyancy resists subduction and asthenosphere flows upward at a flux $Q_b = (h^3/12\mu_{asth})\Delta\rho_{asth}g$. The net vertical entrainment flux Q_E is the difference between these two opposing flux components, i.e. $Q_E = Vh - (h^3/12\mu_{asth})\Delta\rho_{asth}g$. Maximum entrainment as a function of h occurs at $dQ_E/dh = 0 = V - (h_e^2/4\mu_{asth})\Delta\rho_{asth}g$ or $h_e = \sqrt{4\mu_{asth}V/\Delta\rho_{asth}g}$. The resulting flux is $Q_E = 2Vh_e/3$, or twice this value if the subducting slab entrains the asthenosphere on both sides of the slab. The width h_e of the entrainment finger is 20 km for $\mu_{asth} = 10^{19}$ Pa s, $V = 100$ mm year^{-1}, and $\Delta\rho_{asth} = 1\%$, with a corresponding two-sided entrainment flux $E_e = 4Vh_e/3$ which is equivalent to 26 km of asthenosphere subducting as part of the downgoing slab. While this solution geometry assumed vertical subduction and entrainment flow, it also applies to slabs dipping at any angle from the vertical direction (as the buoyancy force and vertical velocity component of the subducting slab depend the same way upon the angle of subduction).

tracer particles to track asthenosphere entrainment on both sides of the subducting slab – for code details, see Rüpke *et al.*'s (2004) paper. In each experiment, the solution region is a 2250 km-wide by 1050 km-deep (oceanic side) or 2500 km-wide by 1300 km-deep (overriding plate side) box, respectively, allowing for a minimum grid-spacing of 4 km in the slab's surroundings. The top boundary is insulating representing the base of the overlying lithosphere, while heat conducts into the slab moving at a fixed 45° angle of subduction. Entrained low-viscosity asthenosphere is assumed to regain the ambient mesosphere viscosity (10^{21} Pa s) after passing deeper than 660 km. The initial asthenosphere layer is taken to be 0.3% compositionally buoyant (due to prior melt extraction) and up to 200°C hotter than underlying mesosphere, resulting in a maximum density reduction of 1%.

The asthenosphere viscosity and subduction rate are then varied in a suite of experiments. Typical asthenosphere flow exhibited in these experiments is shown in Fig. 1(c), which represents an inset near the slab. The experiments from which Fig. 1(c) is taken are shown as two of the videos in the Supplementary Material, which also contains more details of the initial and boundary conditions.

Low viscosity asthenospheric material is entrained on the (hot) bottom side by downdrag only, with the thickness of the entrained sheet ranging from 10 to 55 km, depending upon the asthenosphere's viscosity and buoyancy, and the slab's subduction rate (Fig. 2a). A boundary layer theory was developed to estimate the entrainment beneath the base of the subducting slab (Box 1). This simple theory that neglects conductive heat loss into the slab is in good (>90%) agreement with the numerical results for the moderate to large asthenosphere viscosities (10^{19} up to 10^{20} Pa s) which are numerically best resolved (Fig. 2a). Possibly the growing relative importance of conductive heat loss with decreasing subduction speed is the main reason for the more strongly deviating numerical results at the slowest subduction rates. For the lowest asthenosphere viscosity considered, the boundary layer theory consistently predicts smaller entrainment thicknesses than observed in the numerical calculations, which we think is predominantly an effect of our inability to resolve the predicted very thin entrainment boundary layer with even a 4-km grid, an observation that will be further discussed below. On the cold top of the slab, entrainment is much larger for the same model parameters (Fig. 2b), with roughly twice the entrainment thickness subducting, roughly half by cooling and 'freezing' to the top of the slab and half by downdragging like at the slab's base. If other effects such as the release of fluids from the dehydrating slab significantly reduce the viscosity of the wedge region, then top-side entrainment may be even more completely a 'freezing' instead of 'downdragging' phenomenon.

To verify our numerical techniques and further explore entrainment at the base of a downgoing slab, we also performed several laboratory experi-

....
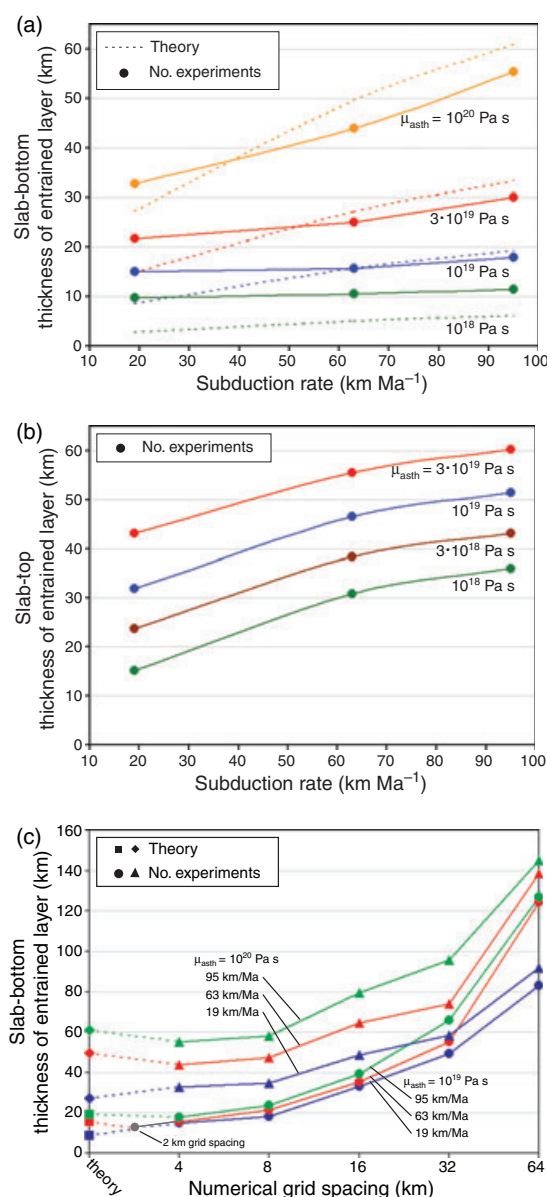
Fig. 2 (a) Thickness of the entrained asthenosphere sheet beneath the base of the subducting slab as a function of slab subduction speed and asthenosphere viscosity. In each experiment, the asthenosphere is assumed to be up to 1% less dense than underlying mesosphere of density 3300 kg m^{-3}, with a gradational base as discussed in Fig. 1(c). Experiments are marked as solid circles, dashed lines are theoretical maxima given by a boundary layer theory (see Box 1). (b) Thickness of the entrained asthenosphere sheet for the slab top-side – same asthenosphere initialization as in (a). Consistently higher entrainment rates are due to the effects of asthenosphere cooling to the top of the slab, which can be as large or even larger than the purely dynamical entrainment effect seen at the base of the slab. (c) Thickness of the entrained asthenosphere sheet at the slab's bottom side as observed in numerical experiments using different numerical grid-spacing. The theoretical maximum thickness (see Box 1) is marked at the 'zero' grid-size edge of the plot. Artificially high asthenosphere entrainment is observed until a fine mesh of ~4 km is used to model flow in the region of the entrained sheet.

ments (Fig. 3). In each experiment, a corn-syrup + water mixture overlay a denser and more viscous pure corn-syrup layer, with the lithosphere boundary simulated by a sheet of plastic moving along a fixed litho-

sphere-slab geometry (angle of subduction 45°). The development of the entrainment boundary layer and tilting of the base of the buoyant asthenosphere towards the subduction zone is shown in Fig. 3 (see also the two videos of laboratory experiments in the Supplementary Material). Numerical calculations using the measured densities and viscosities of the laboratory fluids and the dimensions of the experimental setup can reproduce the laboratory measurements of the entrainment thickness to within our measurement error (< 10%).

Discussion

These magnitudes and modes of predicted slab entrainment are of geological interest. For reasonable asthenosphere density contrasts and viscosities (~0.5–1% less dense and 10^{18}–10^{19} Pa s), the entrained downward flux of asthenosphere is roughly ~20–40% of the downward flux within the lithospheric slab which itself is build up of former asthenosphere, implying that most asthenosphere returns to the deeper mantle by subducting as cold lithosphere instead of being directly downdragged by subducting slabs. This happens because ~60–100 km of former asthenosphere has accreted to form the lithosphere of the subducting slab; both as part of the mid-ocean spreading process (Phipps Morgan, 1994, 1997; Hirth and Kohlstedt, 1996) and as additional conductive thickening of the lithosphere as it cools to a ~100-km-thick thermal boundary layer beneath 100 Ma seafloor (Parsons and Sclater, 1977). The implication is that the asthenosphere is primarily consumed by forming and subducting oceanic lithosphere instead of by direct downward entrainment at subduction zones. In this case, if upwelling mantle plumes supply new asthenosphere at the rate that plate growth and subduction consume asthenosphere, then there should exist a persistent plume-fed asthenosphere layer. The entrainment rates found represent upper rather than lower estimates since our two-dimensional experiments are idealizing an infinitely extended slab in the third dimension, thus not allowing for trench parallel asthenosphere flow or the chance for buoyant asthenosphere to escape around slab edges or through slab
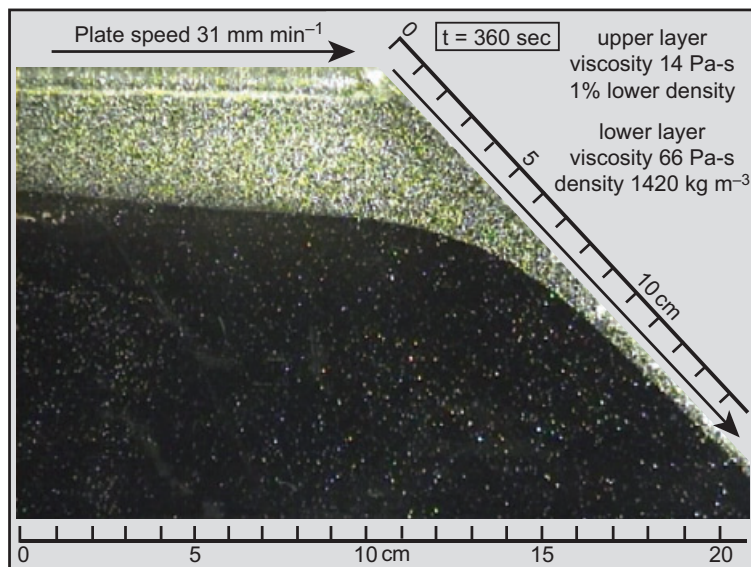
Fig. 3 An example laboratory experiment discussed in the text, shown for the case where the asthenosphere viscosity is 14 Pa s, the density contrast between asthenosphere and deeper layer (66 Pa s, 1420 kg m^{-3}) is ~1%, and the plate 'subduction' speed is 31 mm min^{-1}. The snapshot of the glass-bead rich 'asthenosphere layer' and the deeper glass-bead poor 'mesosphere layer' is shown 360 s after the initiation of the experiment. The predicted pressure-induced tilting of the base of the asthenosphere and the entrainment of a thin asthenosphere sheet between the subducting slab and the higher-viscosity layer are evident. (The full time-history of this run is shown as the *LabMovie31mmpermin.mpg* video in the Supplementary material, where there is also a video of an additional laboratory experiment for a slower plate speed.)

windows. In addition a non-Newtonian (stress-dependent) asthenosphere rheology would further weaken the entrained sheet of asthenosphere, making it more difficult to drag down asthenosphere.

The convection style observed – a thin sheet of asthenosphere entrainment by a subducting slab coexisting with large-scale asthenosphere return flow away from the trench – occurs only when the asthenosphere layer is both less dense and less viscous than the underlying mantle. Changing either asthenosphere density or viscosity alone results in an asthenosphere layer that is easily dragged down and removed by a subducting slab as seen in Fig. 4(b,c), respectively. Figure 4(a) shows the asthenosphere flow that evolves after 20 Ma of plate subduction through a buoyant, low viscosity asthenosphere – the same structure as that seen and analysed previously in Figs 1-3. Figure 4(b) shows the evolution of a system in which a shallow low-viscosity asthenosphere has the same density as its underlying mantle, as could happen if the asthenosphere were not plume-fed and had the same potential temperature and potential density as the underlying mantle. In this case, the whole weak layer is downdragged and removed by plate subduction. Figure 4(c) shows the evolution of a system in which a shallow buoyant layer has the same viscosity (10^{21} Pa s) as its underlying mantle. Here too, the whole buoyant layer is rapidly downdragged and removed by plate subduction. Note that the evolution seen in panels 4(b) and 4(c) is similar to the numerical evolution of panel 4(a) for numerical experiments with a too-coarse (> 8 km) mesh on which slab entrainment cannot be properly resolved – in this case poor numerical resolution leads to runs (cf. panel 4d) that evolve like simulations with entrainment of much higher viscosity asthenosphere. In our numerical experiments, we observed spuriously high entrainment rates until the numerical grid-spacing in the region of the downdragged sheet is less than about 4–8 km (Fig. 2c).

Implications for mantle convection are evident in the differences between the convection scenarios sketched in

Fig. 1(a,b). For geologically reasonable asthenosphere parameters, a plume-fed asthenosphere can form a dynamic low-viscosity boundary layer decoupling the oceanic lithosphere from deeper mantle flow. Indeed the entrained asthenosphere layer may also form a 'lubricating' layer around the slab itself to at least the depth of the 410-km phase transition, an effect that may greatly shape the regional upper mantle flow around a subducting slab, as seen in the detailed flow vectors in Fig. 1(c) or the animation of Fig. 3. As the asthenosphere is then 'consumed' mainly at mid-ocean ridges and by incorporation into the cooling plate, it can form a persistent and geochemically distinct depleted MORB source as proposed by Phipps Morgan and Morgan (1999). The evolution of the asthenosphere wedge beneath an island arc may also be significantly affected by this process. Instead of the 'corner flow' typically assumed beneath an island arc, the arc would be underlain by a buoyant wedge of material that recirculates (see Fig. 1c) and becomes progressively depleted with time until back-arc spreading, a changing subduction geometry, or a pulse of 'fresh' asthenosphere is brought into the back-arc region.

It is important to recognize that none of these effects will be resolvable in global 3-D mantle convection codes until they can incorporate a ~5–10 km numerical resolution of low viscosity regions adjacent to higher viscosity subducting slabs. We think that poor numerical resolution is likely to be the main reason why the asthenosphere entrainment seen in Figs 1, 3 and 4(a) and in the online supplementary videos was not noticed in previous numerical studies exploring asthenosphere–lithosphere dynamics on a global scale. If a numerical experiment's resolution is worse than ~5–10 km, it will tend to improperly entrain too much asthenosphere as a numerical artefact (Figs 2c and 4d), thus generating the scenario sketched in Fig. 1(a) as a consequence of poor numerical resolution. Because of the continuing rapid progress in computational mantle flow, we believe that the computational challenge to successfully include slab entrainment of buoyant asthenosphere will be rapidly overcome.
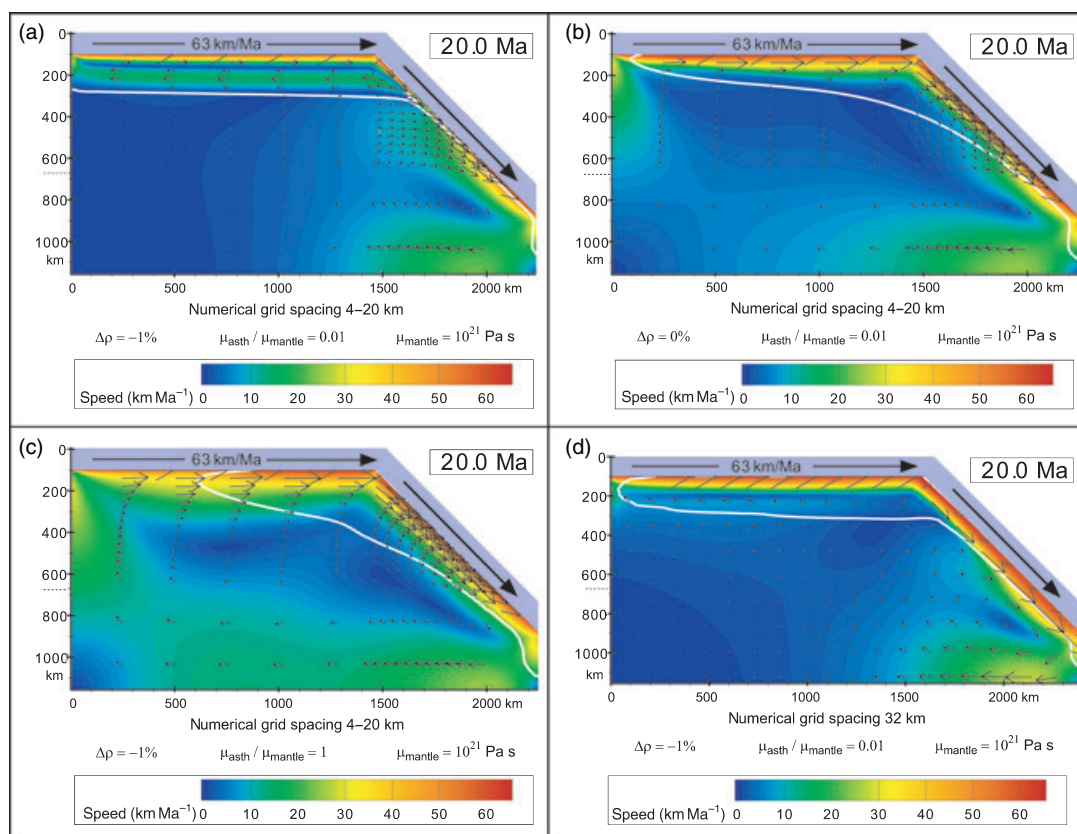
Fig. 4 Comparison of: (a) the dynamics of a buoyant low-viscosity asthenosphere layer; (b) the dynamics of a low-viscosity asthenosphere that has the same density as its underlying mantle; (c) the dynamics of a shallow layer with the same buoyancy contrast as in (a) but for a uniform viscosity mantle. All runs show the evolution after 20 Ma of plate subduction, starting with the same initial conditions apart from differences in viscosity- or density-contrast between the asthenosphere and its underlying mantle. Only the situation in (a) of an asthenosphere that is simultaneously less dense and less viscous (e.g. hotter) than underlying mantle exhibits limited asthenosphere entrainment by slab subduction and the development of classic Schubert&Turcotte-like (Schubert and Turcotte, 1972) asthenosphere return flow away from the trench. Calculations using a too coarse numerical grid (d) cannot resolve a thin entrainment layer and thus tend to drag down too much asthenosphere, resulting in a flow pattern closer to (b) or (c) than to (a), even though calculation (d) used the same physical parameters as calculation (a).

References

Boyd, F.R. and McCallister, R.H., 1976. Densities of fertile and sterile garnet peridotites. *Geophys. Res. Lett.*, **3**, 509–512.

Buck, W.R. and Parmentier, E.M., 1986. Convection beneath young oceanic lithosphere: Implications for thermal structure and gravity. *J. Geophys. Res.*, **91**, 1961–1974.

Dziewonski, A. and Anderson, D.L., 1981. Preliminary reference Earth model. *Phys. Earth Planet. In.*, **25**, 297–356.

Faul, U.H. and Jackson, I, 2005. The seismological signature of temperature and grain size variations in the upper mantle. *Earth Planet. Sci. Lett.*, **234**, 119–134.

Gaherty, J.B., Kato, M. and Jordan, T.H., 1999. Seismological structure of the upper mantle: a regional comparison of seismic layering. *Phys. Earth Planet. In.*, **110**, 21–41.

Goes, S. and van der Lee, S., 2002. Thermal structure of the North American uppermost mantle inferred from seismic tomography. *J. Geophys. Res.*, **107**, ETG2-1–ETG2-13.

Gung, Y., Panning, M. and Romanowicz, B., 2003. Global anisotropy and the thickness of the continents. *Nature*, **422**, 407–411.

Hammond, W.C. and Humphreys, E.D., 2000. Upper mantle seismic wave velocity: effects of realistic partial melt geometries. *J. Geophys. Res.*, **105**, 10975–10986.

Hirth, G. and Kohlstedt, D.L., 1995. Experimental constraints on the dynamics of the partially molten upper mantle: deformation in the dislocation creep regime. *J. Geophys. Res.*, **100**, 15441–15449.

Hirth, G. and Kohlstedt, D.L., 1996. Water in the oceanic upper mantle: implications for rheology, melt extraction, and the evolution of the lithosphere. *Earth Planet. Sci. Lett.*, **144**, 93–108.

Jordan, T.H., 1979. In: *Proceedings of the Second International Kimberlite Confer-* *ence*, Vol. 2 (F.R. Boyd and H.O.A. Meyer, eds). American Geophysical Union, Washington D.C.

Jordan, T.H., 1979. *mineralogies, densities, and seismic velocities of garnet Iherzolites and their geophysical implications.*In: The mantle Sample: Inclusions in Kimberlites and Other Volganics (F.R. Boyd and H.D.A. Meyer, eds), pp. 1–14. American Geophysical Union, Washington D.C.

Karato, S.-I. and Jung, H., 1998. Water, partial melting and the origin of the seismic low velocity and high attenuation zone in the upper mantle. *Earth Planet. Sci. Lett.*, **157**, 193–207.

Karato, S.-I. and Wu, P., 1993. Rheology of the upper mantle: a synthesis. *Science*, **260**, 771–778.

Oxburgh, E.R. and Parmentier, E.M., 1977. Compositional and density stratification in oceanic lithosphere – causes and consequences. *J. Geol. Soc. London*, **133**, 343–355.

Parsons, B. and Sclater, J., 1977. An analysis of the variation of ocean floor bathymetry and heat flow with age. *J. Geophys. Res.*, **82**, 803–827.

Phipps Morgan, J., 1994. The effect of mid-ocean ridge melting on subsequent off-axis hotspot upwelling and melting. *EOS Trans. AGU*, **75**, 336.

Phipps Morgan, J., 1997. The generation of a compositional lithosphere by mid-ocean ridge melting and its effect on subsequent off-axis hotspot upwelling and melting. *Earth Planet. Sci. Lett.*, **146**, 213–232.

Phipps Morgan, J. and Morgan, W.J., 1999. Two-stage melting and the geochemical evolution of the mantle: A recipe for mantle plum-pudding. *Earth Planet. Sci. Lett.*, **170**, 215–239.

Phipps Morgan, J. and Smith, W.H.F., 1992. Flattening of the seafloor depth-age curve as a response to asthenospheric flow. *Nature*, **359**, 524–527.

Phipps Morgan, J., Morgan, W.J., Zhang, Y.-S. and Smith, W.H.F., 1995a. Observational hints for a plume-fed suboceanic asthenosphere and its role in mantle convection. *J. Geophys. Res.*, **100**, 12753–12768.

Phipps Morgan, J., Morgan, W.J. and Price, E., 1995b. Hotspot melting generates both hotspot volcanism and a hotspot swell? *J. Geophys. Res.*, **100**, 8045–8062.

Richter, F.M. and McKenzie, D., 1978. Simple plate models of mantle convection. *J. Geophys.*, **44**, 441–471.

Rüpke, L.H., Phipps Morgan, J., Hort, M. and Connolly, J.A.D., 2004. Serpentine and the subduction zone water cycle. *Earth Planet. Sci. Lett.*, **223**, 17–34.

Schubert, G. and Turcotte, D.L., 1972. One-dimensional model of shallow-mantle convection. *J. Geophys. Res.*, **77**, 945–951.

Shen, Y., Solomon, S.C., Bjarnason, I.T. and Purdy, G.M., 1996. Hot mantle transition zone beneath Iceland and the adjacent Mid-Atlantic Ridge inferred from P-to-S conversions at the 410- and 660-km discontinuities. *Geophys. Res. Lett.*, **23**, 3527–3530.

Sigmundsson, F. and Einarsson, P., 1992. Glacio-isostatic crustal movements caused by historical volume change of the Vatnajökull ice cap. *Geophys. Res. Lett.*, **19**, 2123–2126.

Weertman, J. and Weertman, J.R., 1975. High temperature creep of rock and mantle viscosity. *Annu. Rev. Earth Planet. Sci.*, **3**, 293–315.

Widmer, R., Masters, G. and Gilbert, F., 1991. Spherically symmetric attenuation within the Earth from normal mode data. *Geophys. J. Int.*, **104**, 541–553.

Wiens, D.A. and Stein, S., 1985. Implications of oceanic intraplate seismicity for plate stresses, driving forces, and rheology. *Tectonophysics*, **116**, 143–162.

Supplementary Material

The following material is available at http://www.blackwell-synergy.com: These *.mpg* videos show eight examples of the time evolution of numerical experiments (one each for entrainment on the bottom and top of a subducting slab, two to compare the effects of a sharp and diffuse asthenosphere–mesosphere transition, two in which either the asthenosphere density or viscosity, respectively, is equal to that of the mesosphere, one showing the effects of an inadequate numerical resolution, and one numerical simulation of a laboratory experiment) and two examples of laboratory experiments.

The video *oceanside.mpg* shows 25 Ma of entrainment beneath a plate and slab moving at 63 km Ma^{-1}. The asthenosphere viscosity is 10^{19} Pa s and the underlying mesosphere viscosity is 10^{21} Pa s, with a gradational transition between asthenosphere and mesosphere like that after 50 Ma of heat conduction. Asthenosphere and mesosphere densities are 3270 and 3300 kg m^{-3}, respectively. Below the depth of 660 km, the entrained material is assumed to regain the ambient mesosphere viscosity. (The above parameters are referred to as the 'reference case' in the following.) Video *oceanside_blow-up.mpg* shows 15 Ma of evolution in a zoom of the entrainment region. The oceanward (left) part of Fig. 1(c) is taken after 7 Ma from this numerical calculation.

The video *oceanside_sharp.mpg* shows 25 Ma of entrainment beneath a slab for the same scenario as video *oceanside.mpg*, but with a sharp (discontinuous) asthenosphere–mesosphere transition. There are only small differences between the evolution of experiments with sharp and diffuse asthenosphere-mesosphere transitions. We think this is because asthenosphere entrainment occurs where the top of the asthenosphere meets the subducting slab, for which the 'sharp-transition' and 'diffuse-transition' experiments have the same physical properties.

The videos *oceanside_drho0.mpg* and *oceanside_dmu0.mpg* show the evolution of systems in which the asthenosphere has the same density (3300 kg m^{-3}) or viscosity (10^{21} Pa s) respectively, as the underlying mantle. Figure 4b and 4c are snapshots of these movies after 20 Ma, when the whole asthenosphere is being rapidly down-dragged and removed by plate subduction. This evolution is similar to numerical experiments incorporating an insufficient grid resolution in the region where a sheet of asthenosphere is dragged-down: the video *oceanside_32 km-grid.mpg* shows 25 Ma of time evolution of the reference-case, but using a 32 km numerical grid in this region instead of the 4 km grid-spacing used in all other calculations. The flow field in the asthenosphere is completely different with a much weaker return flow evolving and much more asthenosphere being dragged down by plate subduction. Video *overridingside.mpg* shows 20 Ma of time evolution of asthenosphere and mesophere flow on the top or overriding plate side of the subducting slab for the parameters of our reference-case. In this example the overriding 'landward' plate does not move. The landward (right) part of Fig. 1(c) is taken after 7 Ma from this numerical experiment.

The two videos for the laboratory experiments show examples with identical 'mesosphere' densities and viscosities (1420 kg m^{-3} and 66 Pa s, respectively), and nearly identical asthenosphere densities and viscosities (1% lower density than the mesosphere, viscosities of 12 and 14 Pa-s, respectively). Examples for two different subduction rates are shown, 7 mm min^{-1} (*LabMovie7mmpermin.mpg*) and 31 mm min^{-1} (*LabMovie31 mmpermin.mpg*). Figure 3 shows a static image of the *LabMovie31mmpermin.mpg* video. Video *NumSim_of_Lab3 1mmpermin.mpg* shows the time evolution of a numerical experiment with an initial geometry, plate speed, and viscosity structure chosen to try to match the conditions of the 31mm min^{-1} laboratory experiment. The numerical simulation matches the detailed entrainment thickness and asthenosphere counterflow structures of the laboratory experiment quite well, even matching the time-evolution in deep flow that occurs with the progressive growth of a low-viscosity asthenosphere decoupling zone along the subducting plate interface.